Chemical Engineering Journal 522 (2025) 167863

Contents lists available at ScienceDirect

Chemical Engineering Journal

journal homepage: www.elsevier.com/locate/cej

Ni/Fe-loaded mesoporous KIT-6 enhanced proton transfer for efficient CO_2 desorption

Zhengang Zhou [a], Junjie Zheng [a], Lingyu Shao [b,c,*], Xiao Zhang [a], Chengjin Pan [a], Xiuqi Hu [a], Kai Feng [a], Hao Song [a], Shihan Zhang [b,c], Chenghang Zheng [a,**], Xiang Gao [a,b,**]

[a] State Key Laboratory of Clean Energy Utilization, Institute of Carbon Neutrality, State Environmental Protection Engineering Center for Coal-Fired Air Pollution Control, Zhejiang University, Hangzhou 310027, PR China
[b] Zhejiang Key Laboratory of Clean Energy Conversion and Utilization, Science and Education Integration College of Energy and Carbon Neutralization, Zhejiang University of Technology, Hangzhou 310014, PR China
[c] State Key Laboratory of Advanced Separation Membrane Materials, Zhejiang University of Technology, Hangzhou, 310014, PR China

ARTICLE INFO

Keywords:
Carbon capture
CO_2 desorption
Catalytic solvent regeneration
Acid sites
Solid acid catalyst

ABSTRACT

Catalytic solvent regeneration has garnered significant attention due to its capacity to lower energy demands in industrial processes, promoting broader adoption of carbon capture systems. While progress has been made in catalyst engineering, creating efficient solid acid catalysts still encounters critical obstacles such as synthesizing mesoporous architectures with extensive surface areas and improving the spatial arrangement of active sites. Herein, this study developed a Ni/Fe@KIT-6 catalyst with ordered porosity and dual metal acid sites, leveraging the three-dimensional cubic pore structure of mesoporous silica to enhance liquid-solid mass transfer. The anchored Ni/Fe clusters synergistically enhanced proton transfer, reducing the activation energy of carbamate decomposition through optimized intermediate adsorption configurations. Catalytic testing revealed a 58.1 % enhancement in CO_2 desorption efficiency alongside a 41.2 % decrease in energy requirements relative to non-catalytic systems. The material maintained stable performance across multiple absorption-desorption cycles (efficiency decline <10 %), linked to the KIT-6 framework's retained structural stability and optimized metal-support bonding. Theoretical calculations revealed that the Ni/Fe dual sites lowered the CO_2 desorption reaction energy barrier, aligning with the enhanced CO_2 desorption efficiency. This synergistic interaction of dual metal acid sites within a high-surface-area architecture highlights viable pathways for scalable and energy-efficient CO_2 desorption, thereby advancing practical strategies for large-scale deployment of carbon capture technologies.

1. Introduction

The surging global energy demand and persistent fossil fuel dependence have driven CO_2 emissions to unprecedented levels, exceeding 36.3 Gt annually, primarily from coal (45 %), oil (35 %), and natural gas (20 %) using [1]. This trend has intensified climate impacts, including accelerated sea-level rise and ocean acidification. To tackle these challenges, advancing cost-efficient and low-energy CO_2 capture, utilization, and storage (CCUS) systems has emerged as a pivotal strategy for meeting international climate objectives, particularly in transitioning energy-intensive industries toward sustainability [2–8]. Large-scale CCS technologies, capturing over 90 % of industry CO_2 emissions, play a critical role in mitigating environmental impacts [9–14]. Amine-based chemical absorption, exemplified by monoethanolamine (MEA) systems, achieves over 85 % CO_2 capture efficiency through rapid acid-base reactions [15,16]. However, persistent challenges such as high regeneration energy consumption (3.5–4.5 GJ/t CO_2) limit their economic viability [17]. The amine regeneration process generally requires elevated thermal conditions (>120 °C), constituting more than 60 % of the operational energy consumption in CO_2 capture processes [18], which significantly elevates overall operational expenditures [19–21]. While lowering desorption temperatures could reduce energy penalties, it introduces a trade-off: thermodynamic equilibrium constraints and slower CO_2 desorption kinetics lead to reduced cycling capacity. To

* Corresponding author.
** Corresponding authors at: State Key Lab of Clean Energy Utilization, Zhejiang University, Hangzhou 310027, PR China.
E-mail addresses: slyaimer014@zjut.edu.cn (L. Shao), zhengch2003@zju.edu.cn (C. Zheng), xgao1@zju.edu.cn (X. Gao).

https://doi.org/10.1016/j.cej.2025.167863
Received 22 May 2025; Received in revised form 10 August 2025; Accepted 29 August 2025
Available online 29 August 2025

address equilibrium limitations, strategies such as using advanced amine formulations (e.g., biphasic solvents) or optimizing stripper configurations (e.g., flash strippers, vacuum-assisted systems) have been proposed [22,23]. These technologies are indeed highly effective, and many researchers have already conducted excellent studies in this area. These processes typically focus on enhancing desorption through kinetics or physical means [23,24]. In recent years, catalytic desorption from a thermodynamic perspective has also gained increasing attention, primarily by lowering the reaction energy barrier to enable desorption under milder conditions, thereby reducing the desorption temperature. However, the key challenge remains achieving sufficiently high CO_2 desorption rates at reduced temperatures. Recent studies highlight the potential of catalytic regeneration to accelerate desorption kinetics and lower energy demand simultaneously, bridging the gap between thermodynamic and kinetic barriers [25–27].

Solid acidic catalytic materials offer practical advantages to mitigate operational energy demands in amine-based solvent regeneration processes [28]. Catalytic solvent regeneration achieves temperature reduction during CO_2 desorption by accelerating proton transfer in carbamate decomposition via zwitterion-mediated pathways [18,29]. This mechanism involves proton migration to weaken the C—N bond in carbamate species (R-NH-COO^-), forming a zwitterionic intermediate that facilitates bond cleavage and CO_2 release. The catalytic process benefits from the synergistic effects of dual acid active sites (proton donors and electron acceptors) on the catalyst surface, which maintain transient protonation equilibrium and reduce energy barriers for carbamate breakdown. These dual acid sites exhibit dynamic interconversion through proton transfer mechanisms, a phenomenon critical for modulating proton availability in acid-mediated catalytic cycles. Adjustments in proton concentration directly shift reaction equilibria toward enhanced carbamate fragmentation [30]. Experimental studies confirm that catalysts such as metal oxides [31,32], and carbon-based frameworks [33] achieve a 30 % reduction in MEA solvent regeneration energy consumption via acid-base cooperative effects within CO_2-loaded amine systems.

Catalytic strategies aim to achieve CO_2 desorption below 100 °C, lowering thermal energy input and preserving solvent stability [34]. Transition metal oxides (e.g., ZrO_2, Al_2O_3, CuO, MnO_2, TiO_2) have been prioritized as solid acid catalysts for this purpose due to their surface acidic properties that accelerate carbamate breakdown [35–37]. While oxides like WO_3, MoO_3, and Ag_2O exhibit rapid CO_2 release kinetics, they exhibit partial dissolution during operation, leading to corrosion issues and complicating catalyst recovery [38,39]. In multi-metal oxide systems, the varied electron affinities of constituent metals induce electron redistribution within metal coordination environments, enhancing acid site density and catalytic durability [40,41]. Studies demonstrate that $SO_4^{2-}/ZrO_2/Al_2O_3$ composite catalysts exhibit enhanced catalytic activity compared to single-component metal oxides, attributed to their increased density of acidic active sites [42,43]. This improvement stems from Al-mediated stabilization of sulfate groups and optimized electron density redistribution in Zr—Al coordination clusters, which refine the acidic site environment [35]. Ni/Fe mixed oxides exhibit enhanced alkaline stability compared to monometallic oxides due to their synergistic catalytic effects [44]. Specifically, $NiFe_2O_4$ possesses an inverse spinel configuration, making it an ideal platform for dual-metal active sites that facilitate proton transport in high-pH and elevated-temperature systems [45–47].

However, the restricted specific surface area of conventional catalysts limits active site accessibility, resulting in compromised liquid-solid interfacial contact and thereby impaired proton transfer efficiency within the solvent system [48]. These challenges necessitate the development of catalysts with enhanced specific surface areas and optimized active site distributions to accelerate proton transfer in pathways [34,48,49]. Gao et al. [50,51] developed bifunctional acid-base composite solid catalysts that stabilize active sites under flue gas conditions, achieving 90 % cyclic stability retention over 4 regeneration cycles compared to non-catalytic thermal regeneration systems. The enhanced performance stems from their high surface area (>200 m^2/g) and Brønsted/Lewis acid synergy, as exemplified by ZSM-5/HZSM-5 hybrids and sulfated catalysts like SO_4^{2-}/ZrO_2/SBA-15. These strategies align with emerging catalytic approaches leveraging metal oxides, hierarchical zeolites, and carbon frameworks to strengthen solvent-catalyst interfacial interactions while reducing regeneration energy by 18–30 % [52].

This research pioneers the development of Ni/Fe@KIT-6 mesoporous catalysts to accelerate CO_2 desorption kinetics in MEA-rich solvents and minimize energy consumption during carbon capture at 97 °C. The KIT-6 framework immobilizes $NiFe_2O_4$ nanoparticles, effectively suppressing proton generation and mobility under harsh alkaline and thermal conditions (pH >9, T > 90 °C). Key objectives include: (i) Synthesizing Ni/Fe@KIT-6 catalysts and validating their efficacy in MEA regeneration through acid-base interactions and pore confinement effects, leveraging ordered mesostructures to optimize active site exposure; (ii) Quantifying correlations between desorption dynamics and thermal energy input in low-loading amine systems (0.35–0.5 mol CO_2/mol MEA), aligning with industrial energy benchmarks; (iii) Systematically evaluating catalytic performance via metrics such as CO_2 desorption rate improvement (>40 %), amine capacity retention (>95 %), and regeneration energy savings (>30 %), addressing challenges of metal leaching and structural degradation in conventional catalysts.

2. Experimental

2.1. Reagents

High-purity reagents, including monoethanolamine (MEA, ≥99.9 %), aqueous ethanol (EtOH), 5 % HF solution, nanoscale SiO_2 (purity ≥99.5 %), and $NiFe_2O_4$ (≥99.5 %), were sourced from Shanghai Aladdin Biochemical Technology Co. Ltd. Industrial-grade CO_2/N_2 gases (99 % purity) were supplied by Hangzhou Jingong Gas Co. Ltd., with hydrochloric acid and Pluronic P123 surfactant obtained from Aladdin and Sigma-Aldrich respectively. All liquid phases were formulated with deionized H_2O. These precursors facilitated the fabrication of ordered mesoporous silica (KIT-6) and Ni/Fe@KIT-6 catalysts, with their CO_2 liberation efficiency and MEA regeneration rigorously analyzed in controlled environments.

2.2. Catalyst synthesis

The KIT-6 mesoporous silica was prepared via a modified protocol adapted from established procedures [53]. Initially, Pluronic P123 was dissolved in water and combined with sodium silicate and hydrochloric acid to achieve a uniform solution. This mixture was then homogenized with butanol under continuous agitation. Following sequential addition of sodium silicate, the system underwent hydrothermal aging in a sealed reactor. The resultant solid was isolated by filtration, dehydrated, purified via ethanol-HCl solvent extraction, and thermally activated at 550 °C. For Ni/Fe@KIT-6 synthesis, 0.601 g of the calcined support was evenly suspended in 40 mL ultrapure water under continuous agitation. Subsequently, 0.6 mmol nanoscale $NiFe_2O_4$ (Aladdin, ≥99.5 %) was uniformly incorporated through ultrasonic dispersion (40 kHz, 30 min). Subsequently, 3 mL of glacial acetic acid (≥99 %) was introduced gradually over 5 min. The mixture reacted under mechanical stirring at 25 ± 2 °C for 30 min, resulting in a colloidal dispersion with brown coloration. The resultant material underwent sequential rinsing with a tetrahydrofuran /methanol mixture (3:1 *v*/v) to eliminate organic impurities, followed by thermal drying at 60 °C for 6 h and vacuum desiccation overnight to yield the dark yellow catalyst.

2.3. Material characterization

TEM imaging and *Z*-contrast HAADF-STEM (FEI Talos F200S) were

conducted to resolve nanoscale to atomic-level structural features. Elemental composition was characterized via EDS mapping (FEI Talos F200S). X-ray diffraction analysis (Anton Paar XRDynamic500) elucidated the long-range ordering and crystallinity of the samples. Surface acidity properties, including Brønsted/Lewis acid site quantification, were evaluated using pyridine-adsorbed FTIR spectroscopy (Thermo Fisher Nicolet iS50). Textural parameters, such as specific surface area and porosity, were derived from N_2 physisorption data processed with BET theory (Micromeritics ASAP 2460). Nuclear magnetic resonance (NMR) (AVANCE NEO) and Raman spectroscopy (RS 2010) were applied to monitor real-time changes in amine solution composition during reaction processes. The CO_2 loading in the liquid phase was quantified using a Total Organic Carbon (TOC) analyzer.

2.4. Catalytic performance evaluation

(1) Introduction to the experimental setup

The catalytic performance of mesoporous silica-supported Ni—Fe bimetallic active sites and acidic catalytic materials in accelerating CO_2 desorption kinetics from monoethanolamine-based solvents were quantitatively assessed via desorption experiments, as illustrated in the schematic diagram (Fig. 1). The apparatus integrates a thermally regulated reaction chamber, thermal regulation unit, condensate recovery module, and gas-phase flow control system. The gas flow rate is controlled by the gas mixer, the heating temperature is controlled by the heating controller, the heat input information is obtained from the heat flux signal, and the volume of desorbed CO_2 is monitored by the flow signal collector. A CO_2-saturated MEA solution (100 mL) with an initial CO_2 loading of 0.5 mol CO_2 per mol MEA (deviation range: ±0.01, measurement precision maintained within 1–3 %) was prepared in a thermally controlled reactor under CO_2 partial pressure fixed at 15 kPa. Catalytic desorption was initiated by adding 1.50 g of catalyst (catalyst-to-solution mass ratio: 1.5/100 (*w*/w)) to the solution under continuous mechanical stirring (500 rpm) to ensure uniform heat distribution. CO_2 loading dynamics were monitored by sampling 0.5 mL aliquots at intervals between 0 and 1600 s.

(2) Regeneration energy quantification

The heat duty (HD) for CO_2 desorption was determined via Eq. (1), which integrates solvent-specific reaction thermodynamics and enthalpy balance relationships. Experimental data acquisition was initiated when the MEA solution reached 60 °C, the temperature threshold for CO_2 release. Triplicate measurements of CO_2 loading and MEA concentration ensured experimental reproducibility, with final results reported as averaged values. In the experiment, a 0.5 mL reactor sample underwent TOC analysis (Shimadzu TOC-L, ±0.3 % accuracy) to quantify CO_2 loading, while gas-phase desorption volumes were measured via mass flow meter. Gas-phase CO_2 release kinetics were validated through comparison with aqueous-phase regeneration metrics via TOC analysis to enhance measurement precision, with all tests conducted in triplicate runs. Amine regeneration efficiency was assessed by correlating CO_2 flow rate with regeneration time, while cyclic capacity (CC, mol) – reflecting desorbed CO_2 quality – was derived from liquid-phase measurements using eq. (2):

$$H_{CO_2} = \frac{Q_{CO_2}}{CC_{CO_2}} \tag{1}$$

$$CC_{CO_2} = 10^6 \times M_{CO_2} \times (\gamma_{rich} - \gamma_{lean}) \times C_{MEA} \times V_{MEA} \tag{2}$$

In the formula, H_{CO_2} (GJ/t) represents the CO_2 desorption heat duty; Q_{CO_2} (GJ) represents the heat consumption of CO_2 desorption; CC_{CO_2} (t) represents the CO_2 desorption mass; M_{CO_2} (g/mol) denotes the molar mass of carbon dioxide; γ_{rich} (mol CO_2/mol amine) quantifies the CO_2 capacity in the rich solvent, while γ_{lean} (mol CO_2/mol amine) characterizes the residual CO_2 concentration in the regenerated lean solvent; C_{MEA} (mol/m^3) represents the concentration of solvent; V_{MEA} (m^3) represents the volume of solvent.

3. Results and analysis

3.1. Catalytic enhancement in amine regeneration

The regeneration efficiency of synthesized catalysts was systematically assessed via CO_2 loading dynamics, desorption kinetics, and thermal energy consumption in a 100 mL MEA system. Under standardized conditions (0.53 ± 0.01 CO_2/amine molar ratio, 1.5 wt% catalyst loading), Ni/Fe@KIT-6 demonstrated enhanced catalytic efficacy, attaining a maximum desorption rate of 18.29 mmol·min^{-1} at 93 °C—53 % faster than catalyst-free systems (Fig. 2a-c). Relative to blank, Ni/Fe@KIT-6 achieved a 49.5 % rise in cumulative CO_2 release and 41.2 % reduction in regeneration energy demand at 93 °C, outperforming industry benchmarks at lower operational temperatures. This performance gain arises from Brønsted-Lewis acid dual-site synergy, which facilitates proton mobility and stabilizes metal centers through interfacial charge redistribution, effectively lowering carbamate breakdown activation barriers [54–57]. $NiFe_2O_4$ has a typical inverse spinel structure (AB_2O_4), where Ni^{2+} occupies octahedral sites and Fe^{3+} ions occupy both tetrahedral and octahedral voids. Fine-tuning the oxidation state of the B site in the inverse spinel structure is a robust technique to substantially enhance water-splitting efficiency [54,56]. As show in Fig. 2c, These results demonstrate that Ni/Fe@KIT-6 enhances energy efficiency in carbon capture systems at a relative low desorption

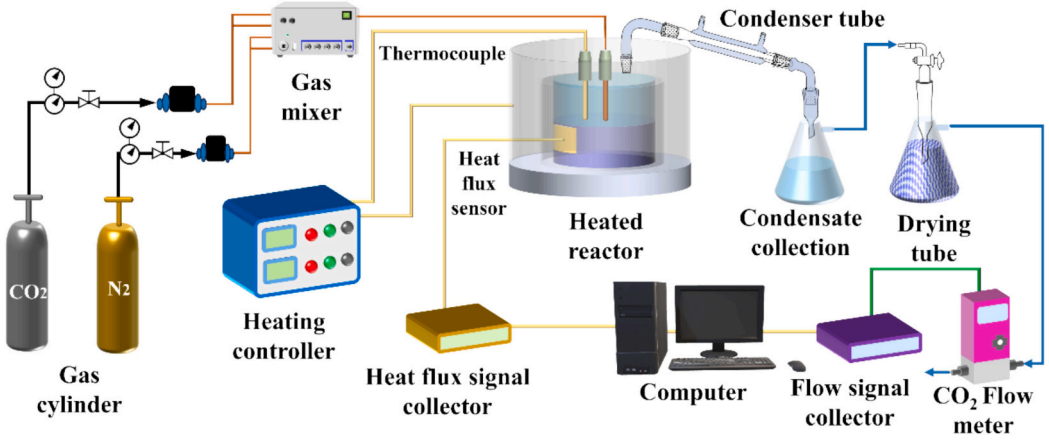

Fig. 1. CO_2 absorption and desorption test bench.

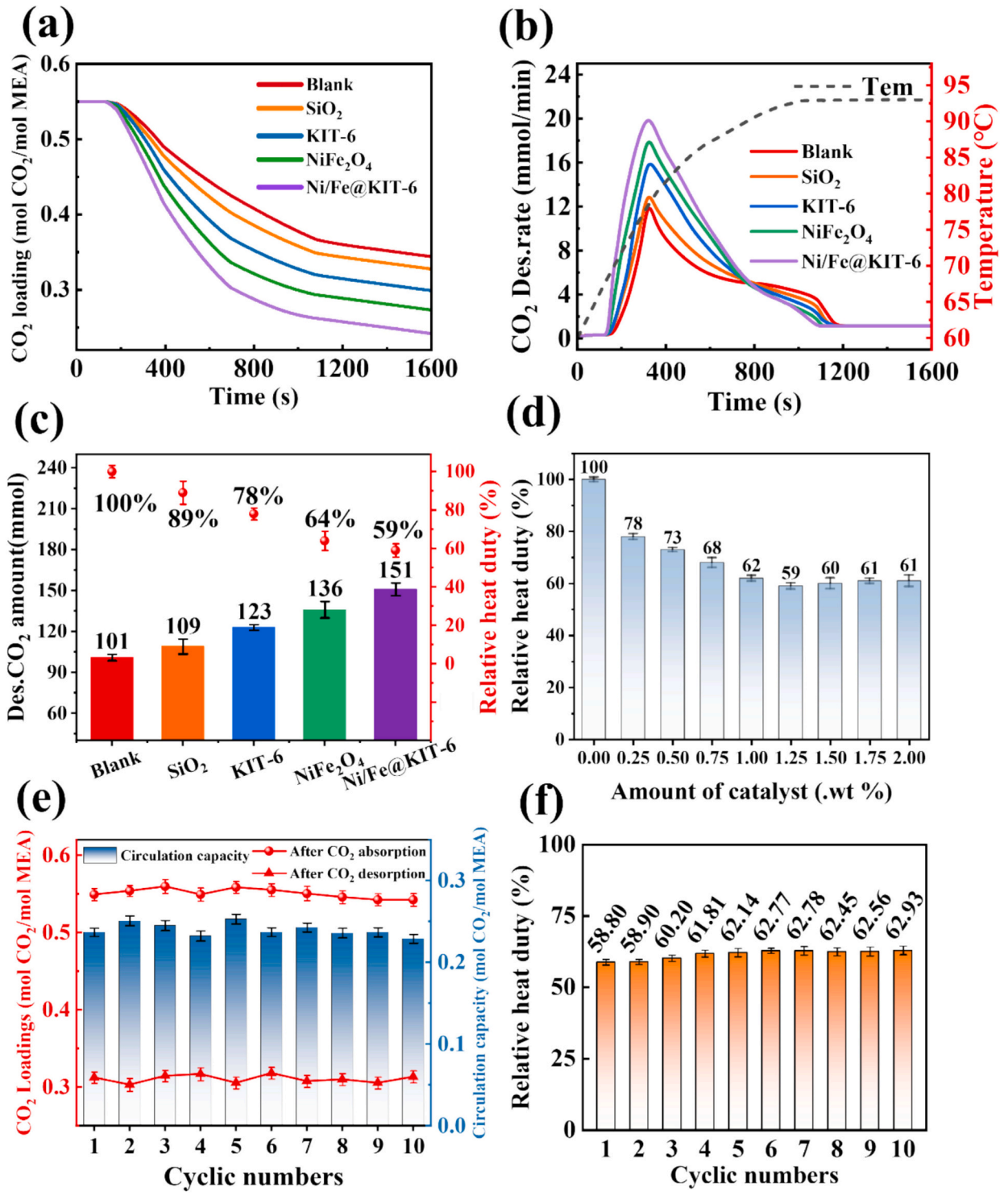

Fig. 2. Evaluation of catalyst-aided MEA regeneration (100 mL system). (a) Solvent regeneration dynamics at 93 °C; (b) CO_2 liberation kinetics with varied catalysts; (c) Cumulative CO_2 release vs. specific thermal energy consumption; (d) Catalyst dosage-dependent thermal load reduction; (e) Cyclic performance and CO_2 capture stability over 10 cycles; (f) Long-term thermal efficiency evolution.

temperature via acid site coupling specific surface area optimization. The synergistic enhancement occurs in catalytic systems due to the presence of multiple catalytic components or materials combined and their various surface and electrochemical features. This effect can lead to improved overall performance compared to the individual components used alone. The improved performance of these high-entropy materials can be attributed to the "cocktail effect". This effect enables the coexistence of various adsorption sites and facilitates the adsorption of multiple intermediates, enhancing the water splitting process [54]. The catalytic mechanism of Ni/Fe@KIT-6 involves dual acid functionalities that facilitate proton exchange through electron donor-acceptor mechanisms. Concurrently, optimized interfacial mass transfer dynamics amplify CO_2 liberation efficiency by improving gas-liquid contact areas.

As illustrated in Fig. 2d, Energy consumption analysis further shows an initial decline followed by stabilization with increasing catalyst dosage, reaching a minimum at 1.25 wt%. In the experiments, the

catalyst was present in powder form within the reactor, and its liquid–solid contact area with the amine solution directly influenced the desorption performance. When the catalyst loading exceeded 1.25 wt%, the extent of liquid–solid contact did not increase linearly with further additions of catalyst. Moreover, the added catalyst also absorbed part of the heat supplied to the reactor. As a result, the variation in desorption energy consumption did not decrease consistently with increasing catalyst loading but instead exhibited a fluctuating trend. As illustrated in Figs. 2e and f, the cycling stability of Ni/Fe@KIT-6 catalysts—a critical parameter for sustainable industrial applications—was rigorously evaluated through 10 consecutive absorption-desorption cycles. The performance during these cycles demonstrated remarkable stability. Although the energy consumption for desorption slightly increased, it remained consistently around 60 %. This resilience at elevated regeneration temperatures underscores the structural robustness of Ni/Fe@KIT-6. Post-reaction characterization revealed that targeted metal redispersion treatments could effectively restore catalytic functionality, confirming the efficacy of the mesoporous framework in stabilizing active Ni/Fe species while ensuring the recyclability of the catalyst for continuous CO_2 desorption in the rich-liquid phase.

Complementary Raman spectroscopy analyses (Fig. 3a and b) elucidated the catalytic enhancement mechanism by tracking molecular vibrations in spent MEA solvents. Critical vibrational modes—O–H bending vibrations (HCO_3^-, 1017 cm^{-1}), symmetric carbonate stretching (CO_3^{2-}, 1065 cm^{-1}), and carbamate C—N vibrations (R–NH–COO^-, 1155 cm^{-1})—showed temporally resolved intensity variations. In non-catalytic systems, HCO_3^- peak intensity diminished gradually, while CO_3^{2-} and carbamate signals showed negligible changes until 1000 s, followed by sluggish decay. In contrast, Ni/Fe@KIT-6-catalyzed systems (Fig. 3b) accelerated the attenuation of all spectral features, evidencing enhanced proton transfer and carbamate decomposition rates through Brønsted-Lewis acid synergy. Figs. 3a and b present a comparison of species changes in the solution under different desorption conditions at the same time. In the desorption conditions with the Ni/Fe@KIT-6 catalyst, the concentrations of HCO_3^-, CO_3^{2-}, and $MEACOO^-$ in the solution are significantly lower, indicating that the catalyst reduces the dissociation difficulty of H_2O, thereby accelerating the desorption reaction rate. According to previous in-situ liquid-phase characterization results, under high CO_2 loading, HCO_3^- is converted to $MEACOO^-$. Due to the higher concentration of HCO_3^-, by the time the concentration of $MEACOO^-$ begins to decrease, a significant amount of $MEACOO^-$ has already been accumulated from the conversion of HCO_3^-. As a result, a very distinct buffering decline region appears during the deep desorption phase. However, Fig. 2b reveals diminishing rate differentials among catalysts post-600 s, attributed to reduced carbamate-catalyst collision frequency as CO_2 loading declines and aqueous-phase mass

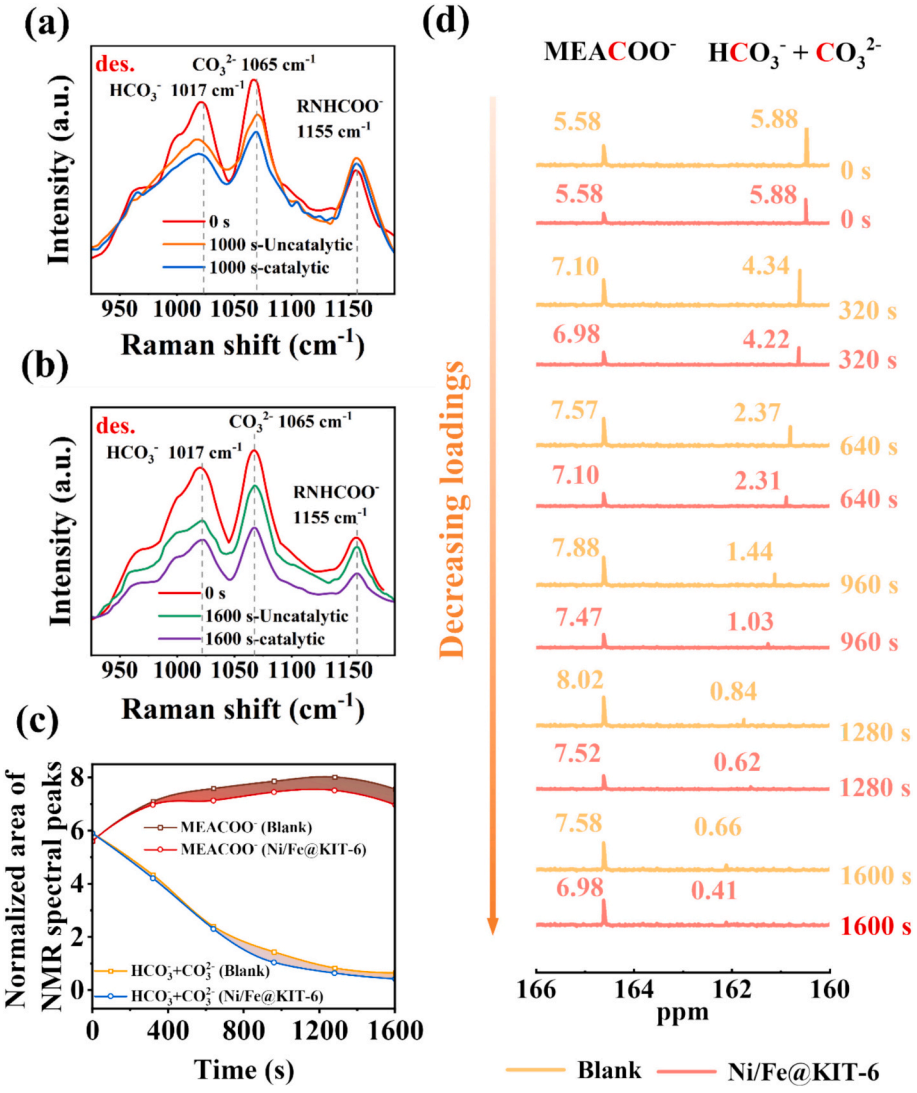

Fig. 3. (a) Baseline (0 s) and post-reaction (1000 s) Raman spectral profiles; (b) Temporal Raman spectral evolution from 0 s to 1600 s; (c) NMR intensity normalization trend; (d) NMR spectral analysis.

transfer limitations emerge. During the desorption process, CO_2 primarily originates from carbamate ($RNHCOO^-$) and bicarbonate (HCO_3^-) ions. Once the temperature exceeds a certain threshold, the CO_2 gas-liquid equilibrium is disrupted, causing the CO_2 loading in the rich solution to decrease as desorption progresses. Because HCO_3^- is more readily decomposed than carbamate, the concentration of HCO_3^- in the solution decreases first. Meanwhile, due to the interconversion between HCO_3^- and carbamate, as the desorption reaction continues, HCO_3^- receives a proton from the amine and converts back to carbamate. However, this conversion occurs at a slower rate. As the absorbent temperature elevates, carbamate species accumulate progressively until attaining the threshold decomposition temperature. At this critical point, the carbamate undergoes accelerated participation in the desorption pathway, triggering a rapid acceleration of CO_2 release kinetics, which subsequently transitions into the equilibrium stabilization stage.

As illustrated in Fig. 3c and d, the mechanistic understanding of CO_2 desorption in MEA solvent was elucidated through ^{13}C NMR analysis of ion speciation under varying CO_2 loadings at 93 °C. The liquid-phase ^{13}C NMR spectra revealed distinct chemical shifts corresponding to carbamate ($MEACOO^-$) and bicarbonate/carbonate (HCO_3^-/CO_3^{2-}) species. At the initial stage of CO_2 desorption (under high loading conditions), partial thermal decomposition of HCO_3^-/CO_3^{2-} species is observed, while a fraction undergoes conversion into $MEACOO^-$ intermediates. This dynamic manifests as a transient rise succeeded by a decline in $MEACOO^-$ concentration (Fig. 3c). Conversely, HCO_3^-/CO_3^{2-} levels exhibit a continuous decline due to their lower thermal stability compared to carbamate, which requires higher energy input for C—N bond cleavage. In later stages (lower CO_2 loading), all ionic species ($HCO_3^-/CO_3^{2-}/MEACOO^-$) contribute to CO_2 desorption. Notably, the Ni/Fe@KIT-6 catalyst systematically reduces the concentrations of these species compared to non-catalytic conditions (Fig. 3c), indicating its role in facilitating $MEACOO^-$ desorption—a primary reactive intermediate—by optimizing its dynamic concentration profile.

Fig. 4 compares the regeneration kinetics, CO_2 desorption capacity, and heat duty of conventional catalytic systems. Experimental data confirm that the novel catalyst synthesized in this work demonstrates superior performance in optimizing CO_2 release and solvent recyclability compared to traditional materials.

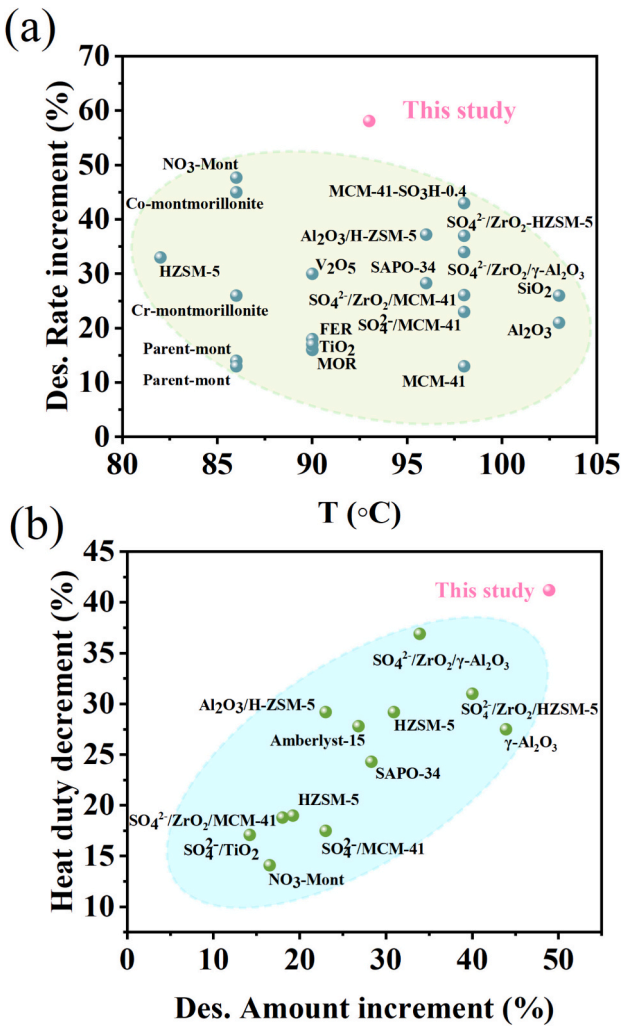

Fig. 4. Benchmark analysis of catalytic CO_2 stripping strategies for solvent regeneration. (a) Temperature-dependent regeneration kinetics enhancement; (b) CO_2 desorption amount increment and heat duty decrement [41,58–67].

3.2. *Effect of various physicochemical properties*

Elucidating the influence of distinct catalyst attributes on their functional behavior is essential to validate their role in regulating CO_2 desorption dynamics and reactive species transformation within the solvent system. This investigation methodically evaluated critical structural attributes of the prepared materials—including metal acid site distribution and pore architecture—to delineate precise relationships between these parameters and their impact on accelerating CO_2 release kinetics. By constructing high surface area mesoporous support catalysts, the liquid-solid contact area is effectively increased, promoting the interaction between the supported metals and the saturated amine solution. This enhances proton transfer within the solution, facilitating the decomposition of carbamate and accelerating CO_2 desorption.

As depicted in Fig. 5a-c, the surface topography of synthesized catalysts was examined via multi-modal electron microscopy techniques to assess morphology, facet orientation, and elemental dispersion. TEM was utilized to characterize the pore architecture, particle morphology of KIT-6, and Ni/Fe distribution in the synthesized catalysts. The TEM and HAADF images confirm the preservation of KIT-6's ordered cubic mesostructure (Ia3d symmetry) post metal impregnation, with Ni/Fe nanoparticles uniformly confined within the interconnected mesochannels. Consistent with theoretical predictions, EDS elemental mapping demonstrated the characteristic spatial distribution of constituent elements, confirming the successful synthesis of Ni/Fe@KIT-6. This spatial confinement promotes strong metal-support interactions between $NiFe_2O_4$ nanoparticles and the KIT-6 framework, significantly improving Ni/Fe dispersion and active site accessibility. This synergistic effect of Fe/Ni has been proven to minimize the aggregation of catalytic particles, thereby increasing the exposed active surface area and facilitating charge transfer [54]. Fig. 5d demonstrates the HAADF-TEM characterization unambiguously resolving phase boundaries between distinct crystallographic orientations. Interplanar distances of 0.25 nm and 0.24 nm in bright/dark contrast zones correspond to the (311) and (222) planes of $NiFe_2O_4$ clusters, respectively . This observation exhibited crystallographic coherence with XRD diffractograms . Intensity line profiles within the region of interest confirmed the spatial dominance of (311) and (222) lattice configurations. Fast Fourier transform (FFT) patterns derived from TEM imaging conclusively validated the prevalence of specific crystallographic surfaces.

Fig. 6a displays the XRD profile of Ni/Fe@KIT-6, where low-angle amorphous scattering signals (~20°) reflect the porous SiO_2 framework. The crystalline phase reflections observed at $2\theta = 35.3°$, 41.7°, 43.4°, 50.8°, 67.7°, and 74.6° are indexed as the (220), (311), (222), (400), (422), and (440) planes, confirming the cubic spinel structure of $NiFe_2O_4$ (JCPDS 86–2267). Notably, the reduced XRD signal intensity compared to pure $NiFe_2O_4$ and pristine KIT-6 reflects the modified crystallinity induced by the Ni/Fe incorporation within the mesoporous matrix. As demonstrated in Fig. 6b, the Brønsted-Lewis acid synergy within the catalyst governs proton-transfer kinetics, thereby reducing

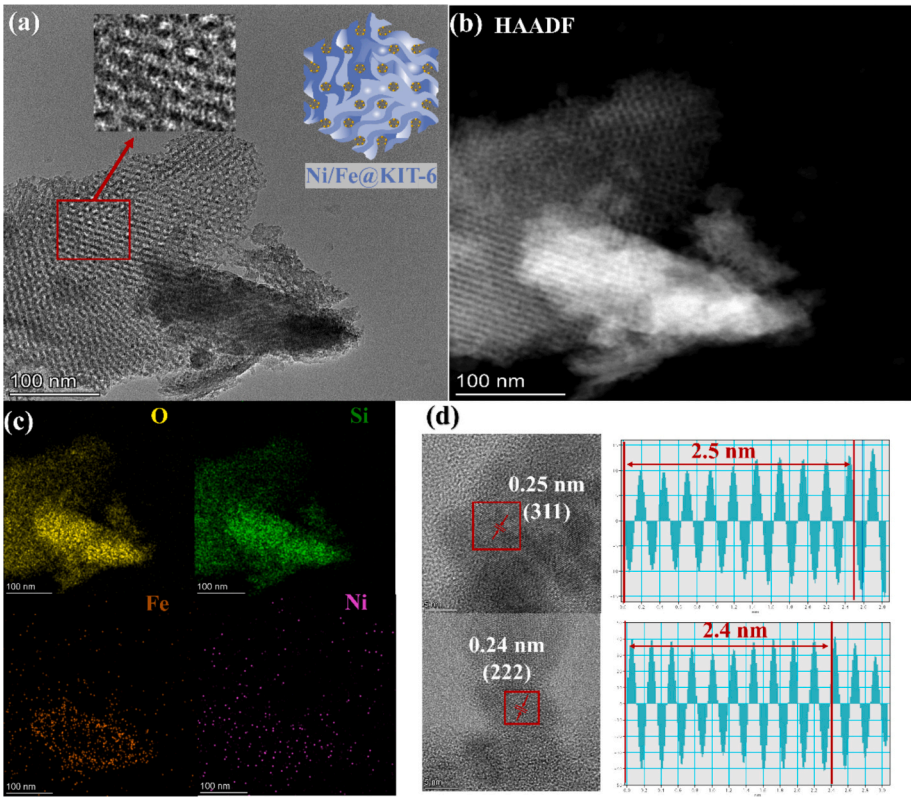

Fig. 5. Structural and compositional analysis of the catalyst. (a) TEM imaging; (b) HAADF-TEM imaging; (c) elemental distribution profiles; (d) FFT pattern analysis of crystalline domains.

the thermodynamic barrier of solvent regeneration. Enhanced Brønsted acidity directly correlates with elevated H^+ ion concentration, which drives the protonation of carbamate species ($RNHCOO^-$) during MEA solvent regeneration through proton transfer mechanisms [68]. Particularly in MEA solutions containing substantial HCO_3^-, Brønsted acid sites synergistically accelerate CO_2 desorption via zwitterion-mediated carbamate decomposition pathways while reducing energy consumption. This structure-activity relationship highlights how targeted modulation of acid site distribution optimizes both energy efficiency and CO_2 release kinetics in solvent regeneration systems. As show in Fig. 6c, notably, the Ni/Fe@KIT-6 exhibited an enlarged average pore diameter (9.35 nm vs. 5.8 nm for pristine KIT-6), attributable to the structural rearrangement induced by optimized metal loading within the mesopores. These structural modifications correlate with enhanced catalytic CO_2 desorption performance through improved active site density and interfacial charge transfer dynamics. As shown in Fig. 6d, KIT-6 demonstrates the highest BET surface area and mesopore volume compared to $NiFe_2O_4$ and SiO_2. All synthesized catalysts displayed characteristic nitrogen physisorption behavior consistent with Type IV isotherms (IUPAC classification), thereby validating their mesoporous structural features. The pronounced hysteresis loops in KIT-6's isotherm reflect its three-dimensional interconnected mesopores, while weaker hysteresis in $NiFe_2O_4$ and SiO_2 suggests reduced mesoporosity. Quantitative analysis reveals KIT-6's surface area ($\geq$450 m^2/g) and balanced mesopore distribution exceed those of $NiFe_2O_4$ and SiO_2 by 10–20-fold, correlating with its superior CO_2 desorption efficiency in aqueous MEA regeneration.

As show in Fig. 6e and f, the product of TAS $\times$ BET shows a linear correlation with CO_2 desorption performance, whereas TAS alone exhibits no significant correlation with CO_2 desorption rate, aligning with prior observations in MEA-based CO_2 desorption systems. This highlights the synergistic role of KIT-6's high surface area (providing accessible active sites) and acid-base functionality in carbamate decomposition kinetics. Crucially, the absence of linear correlation with TAS $\times$ BET with CO_2 desorption rate (Fig. 6f) underscores that bulk acidity metrics alone cannot predict desorption kinetics. Comparative evaluation highlights Ni/Fe@KIT-6's superior efficiency, attributable to its ordered optimized mesostructure (BET surface area: 512 m^2/g) and balanced acid site distribution. In stark contrast, SiO_2's limited performance correlates with its low surface area (43 m^2/g) and insufficient acid site density, emphasizing the critical synergy between textural properties and acid sites in catalytic solvent regeneration.

3.3. DFT calculations and catalytic mechanism

The results presented in Figs. 7a and b reveal that proton donors and acceptors can synergistically enhance CO_2 desorption from MEA solutions via an acid-base catalytic mechanism, with their cooperative interaction being independent of spatial proximity. The proposed model suggests dual catalytic cycles operating in concert - characterized by individualized active sites and coordinated through acid-base equilibrium - drive the observed reaction pathway. Fig. 7a (left) illustrates the proton donor mechanism. During catalysis, the protonated base (Ni/Fe–OH^-) generated under working conditions facilitates directional attraction with the anionic carbamate moiety via charge-dipole interactions. Moderate base strength of this site facilitates proton transfer, enabling carbamate decomposition into CO_2 and the amine. Concurrently, the original Ni/Fe–OH^- site is regenerated and equilibrates with water to reform OH^-, sustaining the catalytic cycle. Owing to their high diffusivity in aqueous media, these hydroxyl anions exhibit dual-site catalytic functionality by synchronizing proton abstraction events between separated active sites through ionic migration [69]. The weakly acidic Ni/Fe–OH^- behaves largely as negatively charged Ni/Fe–OH^- sites under reaction conditions (see the Fig. 6a, right cycle), at which deprotonation of the protonated MEA ($MEAH^+$) can take place. The energy barriers for each reaction step are −0.401 eV, −0.203 eV, and −

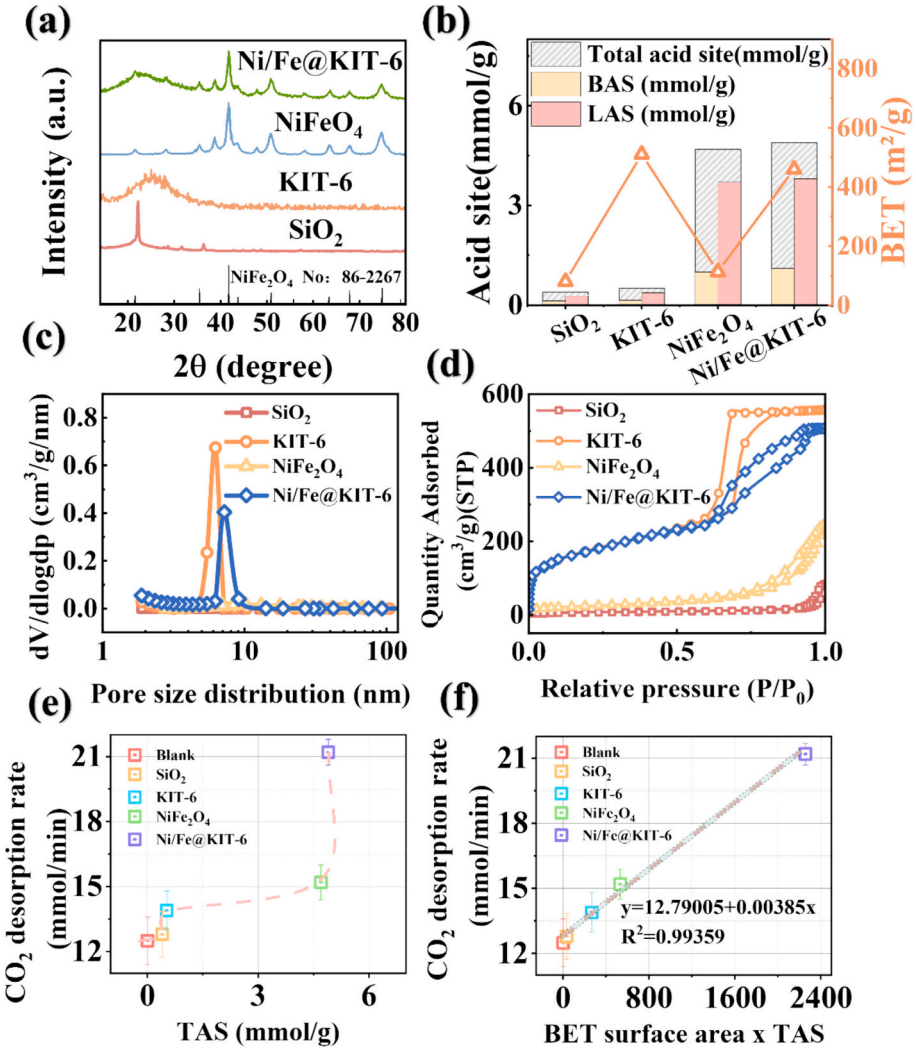

Fig. 6. Catalyst characterization and evolution of the absorption solution during desorption: (a) XRD patterns, (b) acid sites and BET surface area analysis, (c) Mesoporous structure analysis, (d) pore adsorption isotherm analysis, (e) relationship between total acid sites and CO_2 desorption rate (f) correlation of BET surface area × TAS with CO_2 desorption rate.

0.213 eV, respectively. The Ni/Fe–OH^- can be restored upon reaction with OH^-, which was ultimately formed in the first cycle. DFT analyses reveal ammonia solutions predominantly form $MEACOO^-/HCO_3^-$ species that undergo rapid decomposition via Brønsted-Lewis acid site-mediated proton transfer, achieving 73.86 % activation energy reduction versus thermal processes. DFT-based mechanistic analysis establishes a two-stage catalytic cycle for CO_2 conversion on Ni/Fe@KIT-6: (1) zwitterion intermediate formation and (2) carbamate decomposition through concerted acid-base interactions. Critical bond cleavage dynamics arise from the synergistic modulation of carbamate's nucleophilic N/O centers by Brønsted acid (H^+) and unsaturated metal LAS sites, inducing C—N bond elongation and eventual dissociation.

The $RNHCOO^+$ attached to Fe^{n+}/Ni^{n+} had energy differences (ΔE) of −5.644 and − 5.381 eV (Fig. S3), respectively. Furthermore, the ΔE values were − 0.696 and − 0.541 eV during the process attaching H_2O to Fe^{n+}/Ni^{n+} (Fig. S3). The bifurcated reaction pathway (Fig. 6a) involves sequential protonation-deprotonation events. Density functional theory calculations confirm that hydration-derived protons preferentially coordinate to $MEACOO^-$'s nitrogen atom. This coordination triggers hybridization conversion ($sp^2 \rightarrow sp^3$), with concomitant N—C bond elongation (Δd = 0.15 Å) due to partial π-bond character loss. Catalytic solvent regeneration achieves temperature reduction during CO_2 desorption by accelerating proton transfer kinetics during carbamate decomposition through zwitterion-mediated pathways. This mechanism involves proton migration to weaken the C—N bond within carbamate species ($R\text{-}NH\text{-}COO^-$) in organic amine solutions, facilitating low-energy CO_2 release through stabilized transition states.

3.4. Conclusion

Addressing energy-intensive solvent regeneration is pivotal for advancing scalable carbon capture technologies. This study developed a Ni/Fe@KIT-6 catalyst with Brønsted-Lewis acid synergy and ordered mesopores, enabling efficient CO_2 desorption at low temperatures (<100 °C). The dual-metal architecture reduced the carbamate decomposition energy barrier through optimized proton transfer and intermediate adsorption, achieving a 58.1 % increase in CO_2 desorption efficiency and a 41.2 % reduction in regeneration energy compared to non-catalytic systems. The catalyst maintained stable cyclic performance (efficiency decline <10 % over 10 cycles), attributed to the KIT-6 framework's structural integrity and robust metal-support interactions. Sub-100 °C operation aligns with industrial waste heat utilization (60–90 °C), resolving energy competition with conventional high-temperature strippers. This design concurrently lowered steam consumption and stripper unit size, reducing both operational costs and capital expenditures. Future research should prioritize: (1) Durability

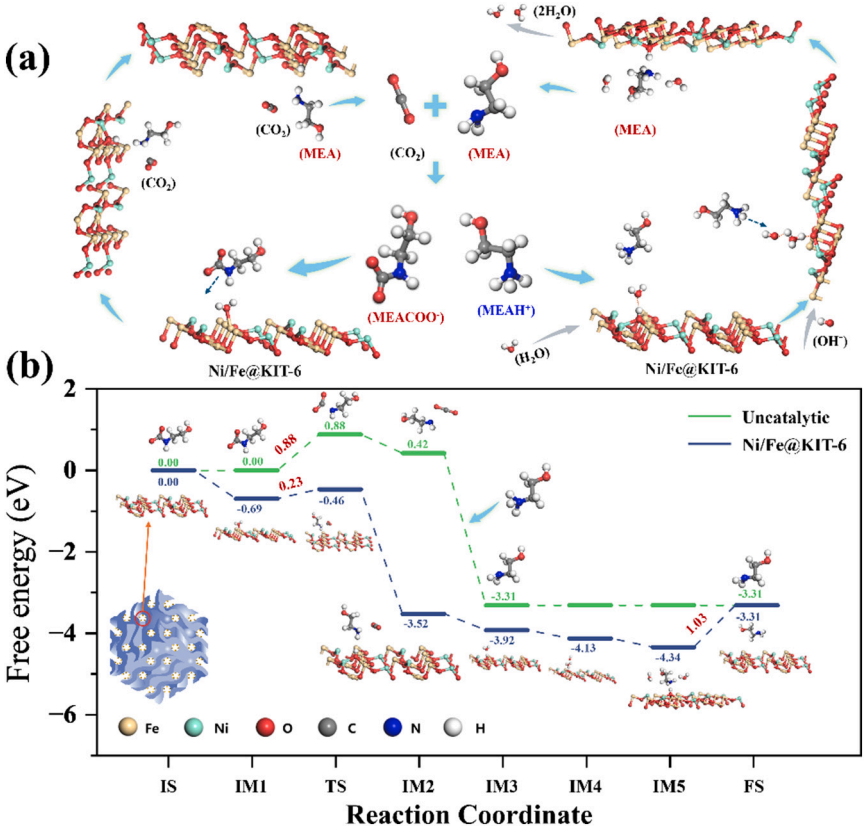

Fig. 7. (a) Proposed catalytic pathway for Ni/Fe@KIT-6 to facilitate MEA-based CO_2 liberation. (b) Energy barriers across reaction pathways under distinct catalytic environments.

enhancement under solvent-induced deactivation (e.g., amine degradation byproducts), (2) Eco-friendly catalyst design integrating low-energy synthesis and recyclability, (3) Reactor optimization to synchronize catalytic performance with industrial thermal management.

CRediT authorship contribution statement

Zhengang Zhou: Writing – review & editing, Writing – original draft, Investigation. **Junjie Zheng:** Investigation. **Lingyu Shao:** Conceptualization. **Xiao Zhang:** Investigation. **Chengjin Pan:** Investigation. **Xiuqi Hu:** Investigation. **Kai Feng:** Investigation. **Hao Song:** Investigation. **Shihan Zhang:** Investigation. **Chenghang Zheng:** Conceptualization. **Xiang Gao:** Conceptualization.

Declaration of competing interest

The authors declare that they have no known competing financial interests or personal relationships that could have appeared to influence the work reported in this paper.

Acknowledgements

This work was supported by the Zhejiang Provincial Natural Science Foundation of China under Grant (No. LDT23E06011E06), National Key Research and Development Program of China (No. 2022YFC3701500) and the “Pioneer” and “Leading Goose” R&D Program of Zhejiang (No. 2023C03156).

Appendix A. Supplementary data

Supplementary data to this article can be found online at https://doi.org/10.1016/j.cej.2025.167863.

Data availability

Data will be made available on request.

References

[1] Z. Deng, B. Zhu, S.J. Davis, P. Ciais, D. Guan, P. Gong, Z. Liu, Global carbon emissions and decarbonization in 2024, Nat. Rev. Earth Environ. 6 (2025) 231–233.
[2] E. Hanson, C. Nwakile, V.O. Hammed, Carbon capture, utilization, and storage (CCUS) technologies: Evaluating the effectiveness of advanced CCUS solutions for reducing CO_2 emissions, Results Surf Interfaces 18 (2025).
[3] P. Wang, Z. Liu, Z. Pan, J. González-Arias, L. Shang, Y. Wang, Z. Zhang, Advances in life cycle assessment of chemical absorption-based carbon capture technologies, Sep. Purif. Technol. 346 (2024).
[4] J. Zheng, Z.R. Chong, M.F. Qureshi, P. Linga, Carbon Dioxide Sequestration via Gas Hydrates: A Potential Pathway toward Decarbonization, Energy Fuel 34 (2020) 10529–10546.
[5] M. Fahed Qureshi, J. Zheng, H. Khandelwal, P. Venkataraman, A. Usadi, T. A. Barckholtz, A.B. Mhadeshwar, P. Linga, Laboratory demonstration of the stability of CO2 hydrates in deep-oceanic sediments, Chem. Eng. J. 432 (2022).
[6] M.F. Qureshi, H. Khandelwal, A. Usadi, T.A. Barckholtz, A.B. Mhadeshwar, P. Linga, CO2 hydrate stability in oceanic sediments under brine conditions, Energy 256 (2022).
[7] M. Aminnaji, M.F. Qureshi, H. Dashti, A. Hase, A. Mosalanejad, A. Jahanbakhsh, M. Babaei, A. Amiri, M. Maroto-Valer, CO2 gas hydrate for carbon capture and storage applications – part 1, Energy 300 (2024).
[8] M. Aminnaji, M.F. Qureshi, H. Dashti, A. Hase, A. Mosalanejad, A. Jahanbakhsh, M. Babaei, A. Amiri, M. Maroto-Valer, CO2 gas hydrate for carbon capture and storage applications – part 2, Energy 300 (2024).
[9] B. Dziejarski, R. Krzyżyńska, K. Andersson, Current status of carbon capture, utilization, and storage technologies in the global economy: A survey of technical assessment, Fuel 342 (2023).
[10] V. Dhamu, X. Mengqi, M.F. Qureshi, Z. Yin, A.K. Jana, P. Linga, Evaluating CO2 hydrate kinetics in multi-layered sediments using experimental and machine learning approach: Applicable to CO2 sequestration, Energy 290 (2024).
[11] V. Dhamu, M.F. Qureshi, S. Abubakar, A. Usadi, T.A. Barckholtz, A.B. Mhadeshwar, P. Linga, Investigating High-Pressure Liquid CO2 Hydrate Formation, Dissociation Kinetics, and Morphology in Brine and Freshwater Static Systems, Energy Fuel 37 (2023) 8406–8420.

[12] K. Jeenmuang, P. Pornaroontham, M. Fahed Qureshi, P. Linga, P. Rangsunvigit, Micro kinetic analysis of the CO2 hydrate formation and dissociation with L-tryptophan in brine via high pressure in situ Raman spectroscopy for CO2 sequestration, Chem. Eng. J. 479 (2024).

[13] V. Dhamu, M.F. Qureshi, T.A. Barckholtz, A.B. Mhadeshwar, P. Linga, Evaluating liquid CO2 hydrate formation kinetics, morphology, and stability in oceanic sediments on a lab scale using top injection, Chem. Eng. J. 478 (2023).

[14] V. Dhamu, M. Xiao, M.F. Qureshi, P. Linga, Deciphering the CO2 hydrates formation dynamics in brine-saturated oceanic sediments using experimental and machine learning modelling approach, Energy 313 (2024).

[15] O.A. Ibigbami, O.D. Onilearo, R.O. Akinyeye, Post-combustion capture and other Carbon Capture and Sequestration (CCS) technologies: A review, Environ. Qual. Manag. 34 (2024).

[16] P. Luis, Use of monoethanolamine (MEA) for CO_2 capture in a global scenario: Consequences and alternatives, Desalination 380 (2016) 93–99.

[17] N. Wang, D. Wang, A. Krook-Riekkola, X. Ji, MEA-based CO2 capture: a study focuses on MEA concentrations and process parameters, Front. Energy Res. 11 (2023).

[18] W. Jiang, Y. Lin, C. Sun, Y. Sun, Y. Zhu, Comparative Review for Enhancing CO_2 Capture Efficiency with Mixed Amine Systems and Catalysts, Molecules 29 (2024).

[19] W.Y. Hong, A techno-economic review on carbon capture, utilisation and storage systems for achieving a net-zero CO_2 emissions future, Carbon Capture Sci. Technol. 3 (2022).

[20] M.M. Jaffar, A. Rolfe, C. Brandoni, J. Martinez, C. Snape, S. Kaldis, A. Santos, B. Lysiak, A. Lappas, N. Hewitt, Y. Huang, A technical and environmental comparison of novel silica PEI adsorbent-based and conventional MEA-based CO_2 capture technologies in the selected cement plant, Carbon Capture Sci. Technol. 10 (2024).

[21] T. Altamash, M. Khraisheh, M.F. Qureshi, Investigating the effects of mixing ionic liquids on their density, decomposition temperature, and gas absorption, Chem. Eng. Res. Des. 148 (2019) 251–259.

[22] A.I. Osman, M. Hefny, M.I.A. Abdel Maksoud, A.M. Elgarahy, D.W. Rooney, Recent advances in carbon capture storage and utilisation technologies: a review, Environ. Chem. Lett. 19 (2020) 797–849.

[23] Y.J. Lin, E. Chen, G.T. Rochelle, Pilot plant test of the advanced flash stripper for CO(2) capture, Faraday Discuss. 192 (2016) 37–58.

[24] F. Rezazadeh, W.F. Gale, Y.-J. Lin, G.T. Rochelle, Energy Performance of Advanced Reboiled and Flash Stripper Configurations for CO2 Capture Using Monoethanolamine, Ind. Eng. Chem. Res. 55 (2016) 4622–4631.

[25] S.Y.W. Chai, L.H. Ngu, B.S. How, Review of carbon capture absorbents for CO2utilization, Greenhouse Gases Sci. Technol. 12 (2022) 394–427.

[26] H. Chu, Z. Huang, Z. Zhang, X. Yan, B. Qiu, N. Xu, Integration of carbon emission reduction policies and technologies: research progress on carbon capture, utilization and storage technologies, Sep. Purif. Technol. 343 (2024).

[27] F. de Meyer, C. Bignaud, The use of catalysis for faster CO2 absorption and energy-efficient solvent regeneration: an industry-focused critical review, Chem. Eng. J. 428 (2022).

[28] X. Zhang, H. Liu, Z. Liang, R. Idem, P. Tontiwachwuthikul, M. Jaber Al-Marri, A. Benamor, Reducing energy consumption of CO_2 desorption in CO_2-loaded aqueous amine solution using Al_2O_3/HZSM-5 bifunctional catalysts, Appl. Energy 229 (2018) 562–576.

[29] A.H. Bhatti, M. Waris, W.W. Kazmi, K.-H. Kang, U.H. Bhatti, Acid-treated activated carbon as simple and inexpensive catalyst to accelerate CO_2 desorption from aqueous amine solution, Carbon Capture Sci. Technol. 8 (2023).

[30] H. Shi, J. Lv, Y. Feng, H. Zhang, Z. Xiong, S. Lu, J. Jin, P. Tontiwachwuthikul, Catalytic CO2 desorption from MEA solution of Al-FeOOH composite catalysts' desorption performance, structure–activity relationship, and new mechanism, Catalysts 14 (2024).

[31] X. Zhang, Y. Huang, H. Gao, X. Luo, Z. Liang, P. Tontiwachwuthikul, Zeolite catalyst-aided tri-solvent blend amine regeneration: An alternative pathway to reduce the energy consumption in amine-based CO_2 capture process, Appl. Energy 240 (2019) 827–841.

[32] Q. Sun, H. Gao, T. Sema, Z. Liang, Enhanced CO_2 desorption rate for rich amine solution regeneration over hierarchical HZSM-5 catalyst, Chem. Eng. J. 469 (2023).

[33] X. Yang, R. Zhou, G. Liu, S. Hussain, Q. Li, Reduce energy consumption for organic amine regeneration by MnOOH/HZSM-5 catalysts, Chem. Eng. J. 493 (2024).

[34] Z.A.S. Bairq, H. Gao, F.A.M. Murshed, P. Tontiwachwuthikul, Z. Liang, Modified Heterogeneous Catalyst-Aided Regeneration of CO_2 Capture Amines: A Promising Perspective for a Drastic Reduction in Energy Consumption, ACS Sustain. Chem. Eng. 8 (2020) 9526–9536.

[35] M. Waseem, M. Al-Marzouqi, N. Ghasem, A review of catalytically enhanced CO_2-rich amine solutions regeneration, J. Environ. Chem. Eng. 11 (2023).

[36] Y. Xu, B. Jin, H. Jiang, L. Li, J. Wei, Investigation of the regeneration of a CO2-loaded ammonia solution with solid acid catalysts: a promising alternative for reducing regeneration energy, Fuel Process. Technol. 205 (2020).

[37] Z. Geng, Y. Yang, Y. Wang, T. Zhu, W. Xu, Catalytic regeneration of amine-based absorbents for CO_2 capture: The effect of acidic sites and accessibility, Sep. Purif. Technol. 327 (2023).

[38] Z. Yang, Y. Shen, H. Yang, H. Yi, H. Guo, X. Zhang, A review of CO_2 catalytic regeneration research based on MEA solution, Front. Energy Res. 11 (2023).

[39] X. Zhang, Z. Zhu, X. Sun, J. Yang, H. Gao, Y. Huang, X. Luo, Z. Liang, P. Tontiwachwuthikul, Reducing Energy Penalty of CO_2 Capture Using Fe Promoted $SO_4^{(2-)}/ZrO_2$/MCM-41 Catalyst, Environ. Sci. Technol. 53 (2019) 6094–6102.

[40] S. Liu, X. Mao, H. Chen, X. Zhu, G. Yang, Catalytic-CO2-desorption studies of BZA-AEP mixed absorbent by the Lewis acid catalyst CeO2-gamma-Al2O3, Molecules 28 (2023).

[41] U.H. Bhatti, S. Nam, S. Park, I.H. Baek, Performance and Mechanism of Metal Oxide Catalyst-Aided Amine Solvent Regeneration, ACS Sustain. Chem. Eng. 6 (2018) 12079–12087.

[42] T. Li, Q. Yu, F. Barzagli, C.e. Li, M. Che, Z. Zhang, R. Zhang, Energy efficient catalytic CO2 desorption: mechanism, technological progress and perspective, Carbon Capture Sci. Technol. 6 (2023).

[43] N. Prasongthum, P. Natewong, P. Reubroycharoen, R. Idem, Solvent Regeneration of a CO_2-Loaded BEA–AMP Bi-Blend Amine Solvent with the Aid of a Solid Brønsted $Ce(SO_4)_2/ZrO_2$ Superacid Catalyst, Energy Fuel 33 (2019) 1334–1343.

[44] Y. Liu, N. Cherkasov, P. Gao, J. Fernández, M.R. Lees, E.V. Rebrov, The enhancement of direct amide synthesis reaction rate over TiO_2@SiO_2@$NiFe_2O_4$ magnetic catalysts in the continuous flow under radiofrequency heating, J. Catal. 355 (2017) 120–130.

[45] A.C.P. Borges, J.A. Onwudili, H. Andrade, C. Alves, A. Ingram, S. Vieira de Melo, E. Torres, Catalytic Properties and Recycling of $NiFe_2O_4$ Catalyst for Hydrogen Production by Supercritical Water Gasification of Eucalyptus Wood Chips, Energies 13 (2020).

[46] J. Zou, Q. Yu, D. Cao, Q. Wang, N. Ma, W. Dai, $NiFe_2O_4$ magnetic nanoparticles supported on MIL-101(Fe) as bimetallic adsorbent for boosted capture ability toward levofloxacin, Mater. Today Chem. 41 (2024).

[47] J. Choi, D. Kim, W. Zheng, B. Yan, Y. Li, L.Y.S. Lee, Y. Piao, Interface engineered $NiFe_2O_4$−x/$NiMoO_4$ nanowire arrays for electrochemical oxygen evolution, Appl. Catal. Environ. 286 (2021).

[48] M.S. Alivand, O. Mazaheri, Y. Wu, G.W. Stevens, C.A. Scholes, K.A. Mumford, Catalytic Solvent Regeneration for Energy-Efficient CO_2 Capture, ACS Sustain. Chem. Eng. 8 (2020) 18755–18788.

[49] X. Hu, Q. Yu, Y. Cui, J. Huang, E. Shiko, Y. Zhou, Z. Zeng, Y. Liu, R. Zhang, Toward Solvent Development for Industrial CO_2 Capture by Optimizing the Catalyst–Amine Formulation for Lower Energy Consumption in the Solvent Regeneration Process, Energy Fuel 33 (2019) 11507–11515.

[50] H. Gao, Y. Huang, X. Zhang, Z.A.S. Bairq, Y. Huang, P. Tontiwachwuthikul, Z. Liang, Catalytic performance and mechanism of SO_4^{2-}/ZrO_2/SBA-15 catalyst for CO_2 desorption in CO_2-loaded monoethanolamine solution, Appl. Energy 259 (2020).

[51] Q. Sun, H. Gao, Y. Mao, T. Sema, S. Liu, Z. Liang, Efficient nickel-based catalysts for amine regeneration of CO2 capture: from experimental to calculations verifications, AICHE J. 68 (2022).

[52] H. Liu, X. Zhang, H. Gao, Z. Liang, R. Idem, P. Tontiwachwuthikul, Investigation of CO_2 Regeneration in Single and Blended Amine Solvents with and without Catalyst, Ind. Eng. Chem. Res. 56 (2017) 7656–7664.

[53] M. Suba, A. Popa, O. Verdeș, S. Borcănescu, P. Barvinschi, Ni and Ce Grafted Ordered Mesoporous Silica KIT-6 for CO_2 Adsorption, Catalysts 12 (2022).

[54] A.A. Krishnan, S. Harikumar, M.A. Aneesh Kumar, R.B. Nair, S. Kurian, M. Ameen Sha, P.S. Arun, NiFe2O4: harnessing catalytic potential in water splitting, Catal. Sci. Technol. 14 (2024) 6155–6175.

[55] N. Kumar, M.R. Ansari, S. Khaladkar, O. Maurya, K.R. Peta, A. Kalekar, M. K. Singha, J.K. Dash, NiFe2O4 nanoparticles as highly efficient catalyst for oxygen reduction reaction and energy storage in supercapacitor, Mater. Chem. Phys. 316 (2024).

[56] V. Manikandan, D. Elango, V. Subash, P. Kumar, J.S. Packialakshmi, P. Jayanthi, Y. J. Sun, K.S. Song, Needle ZrOx loaded NiFe2O4 catalysts for photo-Fenton degradation of bisphenol A and 4 nitrophenol, NPJ Clean Water. 8 (2025).

[57] Z. Liu, B. Tang, X. Gu, H. Liu, L. Feng, Selective structure transformation for NiFe/NiFe2O4 embedded porous nitrogen-doped carbon nanosphere with improved oxygen evolution reaction activity, Chem. Eng. J. 395 (2020).

[58] U.H. Bhatti, A.K. Shah, A. Hussain, H.A. Khan, C.Y. Park, S.C. Nam, I.H. Baek, Catalytic activity of facilely synthesized mesoporous HZSM-5 catalysts for optimizing the CO_2 desorption rate from CO_2-rich amine solutions, Chem. Eng. J. 389 (2020).

[59] X. Zhang, X. Zhang, H. Liu, W. Li, M. Xiao, H. Gao, Z. Liang, Reduction of energy requirement of CO_2 desorption from a rich CO_2-loaded MEA solution by using solid acid catalysts, Appl. Energy 202 (2017) 673–684.

[60] U.H. Bhatti, W.W. Kazmi, H.A. Muhammad, G.H. Min, S.C. Nam, I.H. Baek, Practical and inexpensive acid-activated montmorillonite catalysts for energy-efficient CO_2 capture, Green Chem. 22 (2020) 6328–6333.

[61] N. Ulus, O. Yuksel Orhan, Reduced energy consumption and enhanced CO_2 desorption performance of non-aqueous ionic-liquid-containing amine blends with zeolites, J. Mol. Liq. 359 (2022).

[62] U.H. Bhatti, W.W. Kazmi, G.H. Min, J. Haider, S. Nam, I.H. Baek, Facilely Synthesized M-Montmorillonite (M = Cr, Fe, and Co) as Efficient Catalysts for Enhancing CO_2 Desorption from Amine Solution, Ind. Eng. Chem. Res. 60 (2021) 13318–13325.

[63] T. Wang, W. Yu, F. Liu, M. Fang, M. Farooq, Z. Luo, Enhanced CO_2 Absorption and Desorption by Monoethanolamine (MEA)-Based Nanoparticle Suspensions, Ind. Eng. Chem. Res. 55 (2016) 7830–7838.

[64] Q. Sun, T. Li, Y. Mao, H. Gao, T. Sema, S. Wang, L. Liu, Z. Liang, Reducing Heat Duty of MEA Regeneration Using a Sulfonic Acid-Functionalized Mesoporous MCM-41 Catalyst, Ind. Eng. Chem. Res. 60 (2021) 18304–18315.

[65] H. Shi, A. Naami, R. Idem, P. Tontiwachwuthikul, Catalytic and non catalytic solvent regeneration during absorption-based CO_2 capture with single and blended reactive amine solvents, Int. J. Greenhouse Gas Control 26 (2014) 39–50.

[66] L. Xing, K. Wei, Q. Li, R. Wang, S. Zhang, L. Wang, One-Step Synthesized SO_4^{2-}/ZrO_2-HZSM-5 Solid Acid Catalyst for Carbamate Decomposition in CO_2 Capture, Environ. Sci. Technol. 54 (2020) 13944–13952.
[67] Q. Sun, J. Xiong, H. Gao, T. Sema, W. Olson, Z. Liang, Evaluation of hybrid amines and alcohol solvent with ion-exchange resin catalysts for energy-efficient CO2 capture, Green Chem. 25 (2023) 4647–4655.
[68] G. Vishwakarma, V. Dhamu, M.F. Qureshi, G. Bhattacharjee, T. Pradeep, P. Linga, Understanding the Kinetics of CO(2) Hydrate Formation in Dry Water for Carbon Capture and Storage: X-ray Diffraction and In Situ Raman Studies, ACS Appl. Mater. Interfaces 17 (2025) 4865–4874.
[69] M.F. Qureshi, M. Khraisheh, F. Almomani, Doping amino acids with classical gas hydrate inhibitors to facilitate the hydrate inhibition effect at low dosages, Greenhouse Gases: Sci. Technol. 10 (2020) 783–794.